**PAPER**

# Enhancing thickness determination of nanoscale dielectric films in phase diffraction-based optical characterization systems with radial basis function neural networks

To cite this article: Enes Ataç *et al* 2023 *Meas. Sci. Technol.* **34** 125201

View the article online for updates and enhancements.

# Enhancing thickness determination of nanoscale dielectric films in phase diffraction-based optical characterization systems with radial basis function neural networks

**Enes Ataç**\*⬤, **Anıl Karatay**⬤ and **Mehmet Salih Dinleyici**

Department of Electrical and Electronics Engineering, İzmir Institute of Technology, Urla, İzmir, Türkiye

E-mail: enesatac@iyte.edu.tr

CrossMark

## Abstract

Accurate determination of the optical properties of ultra-thin dielectric films is an essential and challenging task in optical fiber sensor systems. However, nanoscale thickness identification of these films may be laborious due to insufficient and protracted classical curve matching algorithms. Therefore, this experimental study presents an application of a radial basis function neural network in phase diffraction-based optical characterization systems to determine the thickness of nanoscale polymer films. The non-stationary measurement data with environmental and detector noise were subjected to a detailed analysis. The outcomes of this investigation are benchmarked against the linear discriminant analysis method and further verified by means of scanning electron microscopy. The results show that the neural network has reached a remarkable accuracy of 98% and 82.5%, respectively, in tests with simulation and experimental data. In this way, rapid and precise thickness estimation may be realized within the tolerance range of 25 nm, offering a significant improvement over conventional measurement techniques.

Keywords: phase diffraction, neural network, optical fiber sensor, optical characterization, thin dielectric film

(Some figures may appear in colour only in the online journal)

## 1. Introduction

Thin dielectric films are widely used in optical fiber-based sensor technologies as a sensing element or interrogator for various measurements [1–10]. The mentioned studies present applications on gases [1], humidity [2–4], temperature [5, 6], the affinity of molecular interactions [7], pressure [8, 9], geotechnical health [10] etc. To achieve more intelligent sensing capabilities, the particular thin dielectric films are conjuncted with optical fibers which promises the excellent potential for realizing novel sensor concepts [11–13]. Since the sensors' sensitivity and performance strongly relates to the dielectric films' optical properties (e.g. thickness, refractive index) [14, 15], their characterization has become an important and challenging subject in recent years.

In the literature, optical characterization techniques usually depend on interferometric, spectroscopic and ellipsometric techniques [16–22]. However, they are generally complicated and time-consuming procedures for curved surfaces as well as require a sophisticated laboratory environment. Therefore, non-invasive and cost-effective phase diffraction-based

---

\* Author to whom any correspondence should be addressed.

characterization schemes have been exploited for practical applications [23–26]. Nevertheless, the processing of recorded diffraction patterns is usually implemented by classical curve matching methods having some errors from the actual thickness value. Besides, the noisy recorded data show rapid variations due to near-field measurements, causing ambiguity in determining the parameter of interest. Therefore, the application of neural networks to the phase diffraction scheme may be a good approach to enhance the thickness accuracy.

The neural network approaches in the photonics area have received a lot of interest in the last decade by eliminating the need for human intervention, increasing accuracy, and speeding up the process. It has a wide range of application areas in the open literature, including optical distance measurement [27], defect detection [28], event identification [29], strain sensing [30–32], acoustic sensing [33, 34], temperature sensing [35], optical fiber bending measurement [36], optical communication networks [37–39], optical reflectivity measurements [40, 41], tactile sensing [42], leakage detection [43] etc. They have also been used in the thickness characterization of dielectric films due to their importance in fiber optic sensor technologies [44, 45]. In this way, not only the thickness sensitivity of the system is improved but also more accurate and reliable results can be obtained at a level that cannot be obtained with conventional methods.

This study presents an application of the radial basis function (RBF) neural network to improve the thickness sensitivity of phase diffraction-based optical characterization systems. The proposed mathematical and experimental model includes two main parts: (1) phase diffraction and (2) neural network. Initially, the film-coated fiber's diffraction patterns are recorded on the camera. Then, they are converted from 2D to 1D data using feature mapping methods to reduce the computational burden. By leveraging the RBF neural network, we obtain faster and more precise results than conventional curve matching methods, which are less effective for resolving the subtle nanoscale variations in thickness. Moreover, through a detailed parametric sweep, we achieve a sensitivity range of 25 nm with sufficient accuracy. To assess the robustness of our approach, we explore the effect of noise on our numerical model using Poisson and Gaussian distributions. Specifically, we obtain high accuracy of 98% when tested on synthetic data, whereas this rate is seen as 82.5% when noisy experimental data is used. To further assess the impact of our approach, we make a comparison with the widely-used linear discriminant analysis (LDA) method, which is a linear fitting approach different from neural network algorithms. Our results show that the accuracy of LDA drops to 47% when using 25 nm classes, thus highlighting the superior performance of our RBF neural network approach in improving thickness resolution.

The organization of the article is as follows. Section 2 provides the readers with the essential background information necessary to understand the proposed methodology. The intricate experimental setup, including the coating procedure and the measurement methodology, is elucidated in section 3. In section 4, we present the results obtained using the proposed methodology, along with their detailed analysis and discussion. The scanning electron microscopy (SEM) images are also presented for verification. The concluding remarks are given in the last section.

## 2. Proposed method

The proposed model is mainly interested in neural network application for the thickness estimation of dielectric films coated on optical fibers. It can be divided into two main parts: (1) plane wave-based phase diffraction from film-coated optical fiber via paraxial ray tracing and (2) application of RBF network to noisy near field diffraction pattern acquired by the sensor array. The general scheme of optical system and neural network is given in figure 1.

As seen from the figure 1(a), every point of the incident wavefront is exposed to different phase delays due to the curved geometry while traversing the three-layer geometry. Therefore, the plane wavefront is discretized to the sections represented by rays. Every ray is paraxially traced and the acquired phase through the phase object can be represented as:

$$
\begin{aligned}
U(x') &= A(x')e^{ikz}e^{-i\phi_s}, \quad |x'| > c \\
U(x') &= A(x')e^{ikz}e^{-i[\phi_s+\phi_d]}, \quad b < |x'| < c \\
U(x') &= A(x')e^{ikz}e^{-i[\phi_s+\phi_d+\phi_{cl}]}, \quad a < |x'| < b \\
U(x') &= A(x')e^{ikz}e^{-i[\phi_s+\phi_d+\phi_{cl}+\phi_{co}]}, \quad 0 < |x'| < a
\end{aligned}
\tag{1}
$$

where $a$, $b$ and $c$ are the core, the cladding and the coated optical fiber radii, respectively. Besides, $\phi_s$, $\phi_d$, $\phi_{cl}$ and $\phi_{co}$ are the optical paths given in [24]. Since the phase is more sensitive than amplitude of the field, the amplitude of plane wave $A(x')$ is assumed unity for the simplicity.

In the end, the diffracted field at point $P$ on the sensor array at a distance $z$ is calculated according to the near field Huygens–Fresnel diffraction formula as [46]:

$$
U'(P) = -\frac{1}{4\pi} \sum_{x'=-\infty}^{\infty} \left( ik(1+\cos\theta) - \frac{\cos\theta}{r} \right) \frac{e^{ikr}}{r} U(x')
\tag{2}
$$

where $\cos\theta$ is the obliquity factor. The intensity can be found by taking the absolute square of the diffracted field by equalizing the total power on the detector to unity.

Once the normalized intensity is obtained on the sensor array, the neural network part starts. The general overview of the neural network is given in figure 1(b). The recorded 2D intensity consists of 1D diffraction patterns. By mapping these diffraction patterns to the RBF neural network having simpler structure and faster learning speed [47], the algorithm is trained with synthetic data. The network consists of three layers: input layer, hidden layer, and output layer. The input layer spans the *n*-dimensional input vectors. Non-linear RBFs are used in the hidden layer. At the output of the network, the data is a linear combination of input and RBFs. The scalar expression for the output of the system can be written as:

$$
y(x) = \sum_{j=1}^{M} w_j f(||\mathbf{x} - \mathbf{c_j}||) + w_0
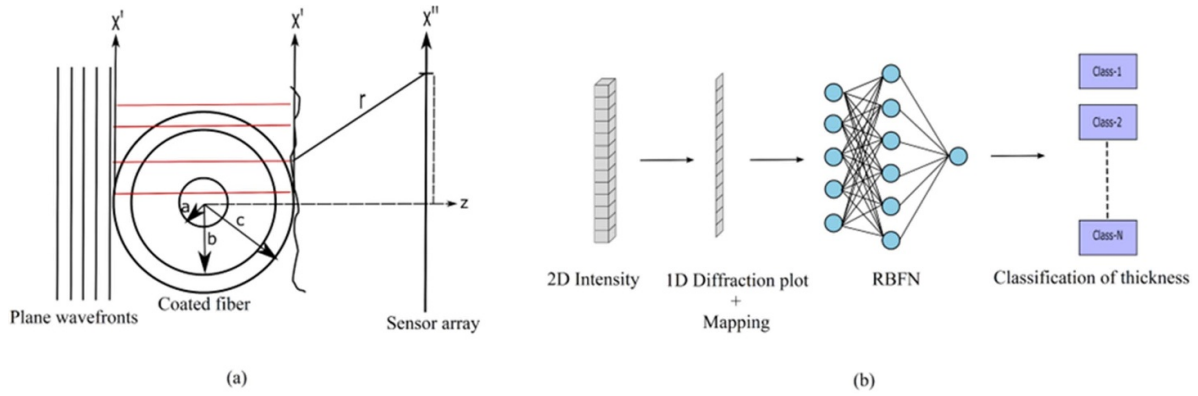\tag{3}
$$

**Figure 1.** (a) The diffraction geometry from coated optical fiber (b) illustration of RBF Neural Network.

where $M$ denotes the number of neurons, $\mathbf{x} = [x_1 \ x_2 \dots]$ indicates the input vector, $w_j$ is the weight of the related neuron, $w_0$ means the weight of the bias, $f$ and $\mathbf{c_j} = [c_{j1} \ c_{j2} \dots]$ indicate the RBF, and the center vector of the related neuron, respectively. $||.||$ means the Euclidian norm in the vector space. The RBF, which depends only on distance, is usually Gaussian and can be expressed as equation (5). Gaussian RBFs (GRBF) are smooth, localized, and have a universal approximation property, making them well-suited for modeling complex functions with localized patterns [48]. Since we are interested in a large circular phase object in our model that causes diffraction of the input field, and the diffraction integrals usually lead to Gaussian-like functions [49, 50], GRBFs are chosen.

$$f(||\mathbf{x} - \mathbf{c_j}||) = e^{-\frac{||\mathbf{x} - \mathbf{c_j}||^2}{2\sigma_i^2}} \tag{4}$$

where $\sigma_i$ is the centrality distance. The most straightforward scheme for training RBF neural networks is to take a set of center values that are randomly chosen from training. Then it uses fixed-width functions and trains the weights to linear output units [51]. This process can be done iteratively to minimize the error. The mean squared error, to be minimized, is expressed as follows [52].

$$MSE = \frac{1}{N} \sum_{i=1}^{N} (y_i - \hat{y}_i)^2 \tag{5}$$

where $y_i$ denotes the actual value, $\hat{y}_i$ is the predicted value, and $N$ means the number of samples. If the MSE goes below the user-defined value, the iteration is terminated and the final output value is predicted.

## 3. Experiment

The polymer-coated optical fiber is chosen as a three-layer geometry phase object having known optical properties such as refractive index and radii. Since we want to exert nanometer precision and stability over the thickness of multi-layer films, the prominent technique layer by layer Assembly is

selected for the coating procedure [53–55]. A combination of Polyacrylic acid and polyethylenimine was used in the experiment. We can obtain desired multi-layer coating thickness by creating positive and negative charged layers via repeating dipping and drying processes, respectively.

The illustration of experiment setup and laboratory photo is given in figure 2. The experimental setup begins with the generation of plane wave via conversion of 632.8 nm He–Ne laser with a beam expander. Then, the plane wave was sent to the polymer-coated optical fiber. After the plane wave diffracts from the phase object on the sensor array, the near field diffraction pattern is recorded. The sensor array has 1.12 µm pixel size. The distance between phase object and sensor array is 600 µm and the radius of core and cladding are $a = 4.15$ µm and $b = 62.5$ µm, respectively.

After the recorded intensity pattern is obtained from the sensor array, the RBF neural network algorithm is applied. Diffraction patterns are generated through the numerical simulations using the formulations in the previous section. These generated data are used for training purposes, and each vector is matched with a thickness value. Some of the generated data is used for testing so that the number of neurons needed, and the required mean squared error target can be determined. Then, the numerical simulation data are trained with a RBF network and the experimental data were tested over this network. Then the recorded patterns are classified and the thickness value of the dielectric films can be predicted. At the end, thickness value of dielectric films are verified by SEM.

## 4. Results and discussion

In this study, we set our sights on the intricate detection of coating thickness beyond the limits of classical diffraction theory. For this reason, the neural network is trained up to 450.5 nm to cover all coating thickness ranges. To this end, we generated data using Matlab software, producing a comprehensive dataset featuring 0.5 nm increments between 0 nm and 450.5 nm coating thickness. Each dataset contains 137 units; however, due to the symmetry of the generated data, we reduced the length of the samples to 74 units. Out of 901
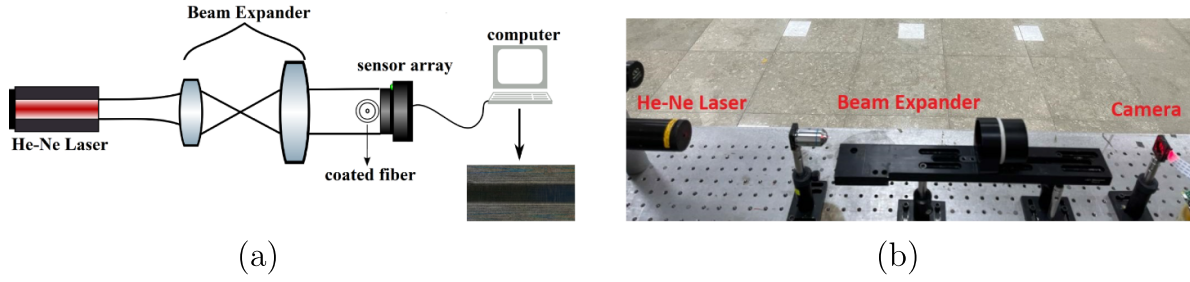
**Figure 2.** The experimental setup (a) illustration (b) laboratory photo.

**Table 1.** The accuracy rate of the neural network approach for MSE $= 10^{-2}$.

|      | 5    | 10   | 25   | 50   | 150  | 225  |
| ---- | ---- | ---- | ---- | ---- | ---- | ---- |
| 10   | 0.10 | 0.24 | 0.54 | 0.84 | 0.98 | 1.00 |
| 20   | 0.41 | 0.68 | 0.90 | 0.98 | 1.00 | 1.00 |
| 30   | 0.82 | 0.92 | 0.97 | 0.99 | 1.00 | 1.00 |
| 40   | 0.89 | 0.95 | 0.97 | 0.99 | 1.00 | 1.00 |
| 50   | 0.91 | 0.95 | 0.98 | 0.99 | 1.00 | 1.00 |
| 60   | 0.91 | 0.96 | 0.98 | 0.99 | 1.00 | 1.00 |
| 70   | 0.90 | 0.96 | 0.98 | 0.99 | 1.00 | 1.00 |
| 80   | 0.90 | 0.96 | 0.97 | 0.99 | 1.00 | 1.00 |
| 90   | 0.90 | 0.96 | 0.97 | 0.98 | 1.00 | 1.00 |
| 100  | 0.90 | 0.94 | 0.98 | 0.99 | 1.00 | 1.00 |
| 110  | 0.90 | 0.95 | 0.97 | 0.99 | 1.00 | 1.00 |
| 120  | 0.90 | 0.95 | 0.96 | 0.99 | 1.00 | 1.00 |
| 130  | 0.88 | 0.95 | 0.90 | 0.99 | 1.00 | 1.00 |
| 140  | 0.89 | 0.89 | 0.90 | 0.93 | 1.00 | 1.00 |
| 150  | 0.89 | 0.88 | 0.98 | 0.95 | 1.00 | 1.00 |
| 160  | 0.88 | 0.89 | 0.97 | 0.88 | 1.00 | 1.00 |
| 170  | 0.88 | 0.84 | 0.98 | 0.88 | 1.00 | 1.00 |

generated datasets, we utilized 451 fixed data for training and 450 for testing. We optimized the parameters for the RBFs, selecting a spread value of one and incrementally adding 25 neurons between displays. The maximum number of neurons and mean squared error goal are determined through parametric sweeps, and the results are presented in tables 1 and 2. These tables highlight the variation in coating estimation sensitivity and the number of neurons for two different mean squared error goals. In these tables, the first column and the first row correspond to the maximum number of neurons and classification sensitivity in the classes, respectively. The sensitivity values are classified into six categories, with the 25 nm sensitivity range designated as the first class, the 25.5–50 nm sensitivity range as the second class, and so forth. We progressively increase the number of neurons in the hidden layer in ten-step increments, up to a maximum of 170. In cases where the number of neurons was limited to 10, the accuracy was insufficient. However, by gradually increasing the number of neurons, we ultimately achieved the desired level of accuracy.

The overarching objective of this investigation is to maintain a consistently high level of accuracy throughout the testing phase. Therefore, we employed a neural network architecture of no fewer than 20 neurons to achieve 25 nm sensitivity. Notably, this choice of neural network structure is consistent across both mean squared error goal tables. To thoroughly analyze our method's performance, we create classes specifically designed to achieve the aforementioned sensitivity value. For a meaningful comparison, we also implement a linear discrimination analysis simulation, which similarly constructs classes according to different sensitivity values using the same data. Remarkably, the performance of the latter method is found to be relatively lackluster, achieving a meager 47% accuracy for 25 nm sensitivity, as detailed in table 3.

In the network, we used synthetic data for training and experimental data for testing where measurement data often contain additional noise, such as shot and thermal noise, which differ from the simulated data. Therefore, we carried out numerical simulations incorporating thermal noise via the Gaussian distribution and shot noise via the Poisson distribution. As shown in figure 3(a), RBF and LDA algorithms give approximately the same results for low signal-to-noise ratio (SNR) values. It can be seen that the accuracy rate between the output validation data and the test target data increases with the help of RBF for SNR values of about 30 dB and above. To see similar performance in LDA, the SNR should exceed 120 dB. The RBF algorithm yields better results as the MSE goal decreases despite low accuracy at low SNR values due to over-training. Besides, we model the synthetic data with the Poisson distribution. Since the test data are mapped between

**Table 2.** The accuracy rate of the neural network approach for MSE $= 10^{-3}$.

|     | 5    | 10   | 25   | 50   | 150  | 225  |
|-----|------|------|------|------|------|------|
| 10  | 0.10 | 0.24 | 0.54 | 0.84 | 0.98 | 1.00 |
| 20  | 0.41 | 0.68 | 0.90 | 0.98 | 1.00 | 1.00 |
| 30  | 0.82 | 0.92 | 0.97 | 0.99 | 1.00 | 1.00 |
| 40  | 0.89 | 0.95 | 0.97 | 0.99 | 1.00 | 1.00 |
| 50  | 0.91 | 0.95 | 0.98 | 0.99 | 1.00 | 1.00 |
| 60  | 0.91 | 0.96 | 0.98 | 0.99 | 1.00 | 1.00 |
| 70  | 0.90 | 0.96 | 0.98 | 0.99 | 1.00 | 1.00 |
| 80  | 0.90 | 0.96 | 0.97 | 0.99 | 1.00 | 1.00 |
| 90  | 0.90 | 0.96 | 0.97 | 0.98 | 1.00 | 1.00 |
| 100 | 0.90 | 0.94 | 0.98 | 0.99 | 1.00 | 1.00 |
| 110 | 0.90 | 0.95 | 0.97 | 0.99 | 1.00 | 1.00 |
| 120 | 0.90 | 0.95 | 0.96 | 0.99 | 1.00 | 1.00 |
| 130 | 0.88 | 0.95 | 0.90 | 0.99 | 1.00 | 1.00 |
| 140 | 0.89 | 0.89 | 0.90 | 0.93 | 1.00 | 1.00 |
| 150 | 0.89 | 0.88 | 0.98 | 0.95 | 1.00 | 1.00 |
| 160 | 0.88 | 0.89 | 0.97 | 0.89 | 1.00 | 1.00 |
| 170 | 0.88 | 0.84 | 0.98 | 0.86 | 1.00 | 1.00 |

**Table 3.** The accuracy rate of the linear discriminant analysis.

| Sens. (nm) | 5    | 10   | 25   | 50   | 150  | 225  |
|------------|------|------|------|------|------|------|
| Accu.      | 0.17 | 0.30 | 0.47 | 0.52 | 0.66 | 0.82 |
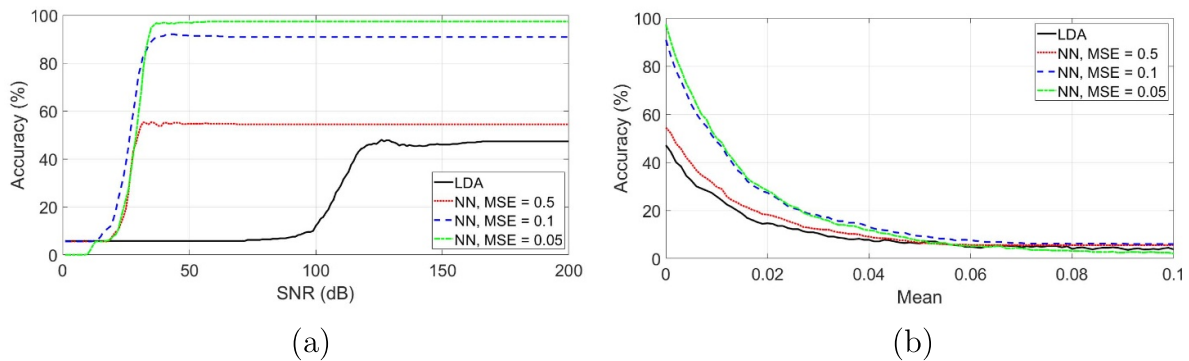


**Figure 3.** Effect of noise on the accuracy rate of neural network with various MSE goals and LDA (a) accuracy versus SNR of AWGN (b) accuracy versus mean of Poisson noise.

0 and 1, the Poisson distribution noise's mean is also adjusted not to exceed 0.1. As demonstrated in figure 3(b), the accuracy decreases for all algorithms and MSE goal values as the noise power increases. The most successful result is obtained at low noise for MSE $= 0.05$. To see the effect of additive white Gaussian noise (AWGN) and Poisson distributed noise combinations, we add them together. Two cases for Poisson distribution noise, for the mean value 0.001, are given in figure 4. The accuracy is investigated for parametrically increased SNR value of the AWGN channel. The dB values, where the accuracy value jumps abruptly, coincide with approximately the same points. However, a decrease is observed in the maximum accuracy values reached.

In the case of MSE $= 0.05$, the accuracy is lower than LDA in the low SNR region due to overfitting. At low SNRs, the data points are more dispersed and have fewer distinct clusters, making it challenging for an RBF classifier to separate the classes accurately. Regularization helps by introducing constraints to the model, making it less noise-sensitive and reducing overfitting. We utilized Ridge regularization with a ridge parameter that determines the strength of regularization applied to the model. Random search technique was used to explore a range of ridge parameter values during cross-validation. When regularization is applied with an appropriate ridge parameter value, it is observed that this approach improves the accuracy up to 22% in the low SNR region whereas, degrading the accuracy in the high SNR region. The model already captures the underlying patterns in the data effectively without additional regularization in high SNR scenarios. When regularization is applied in this
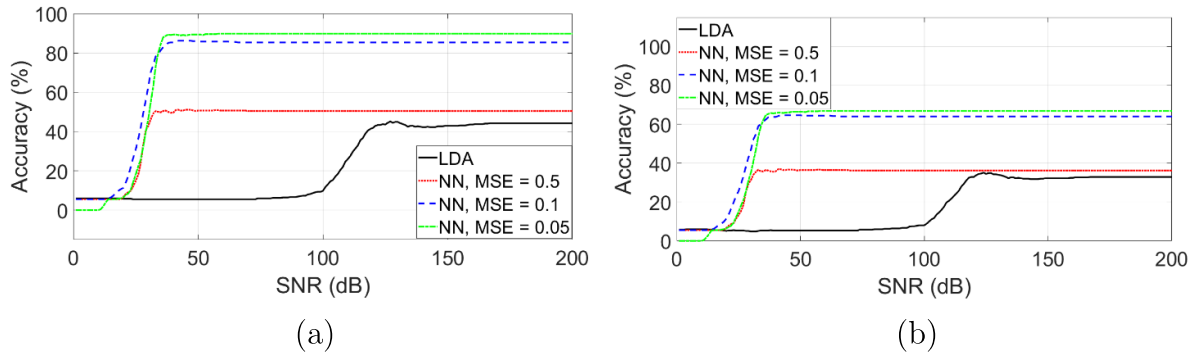
**Figure 4.** Effect of both Poisson distributed shot noise and Gaussian distributed thermal noise (a) mean of Poisson distribution is 0.001 with varying SNR for Gaussian noise (b) mean of Poisson distribution is 0.005 with varying SNR for Gaussian noise.
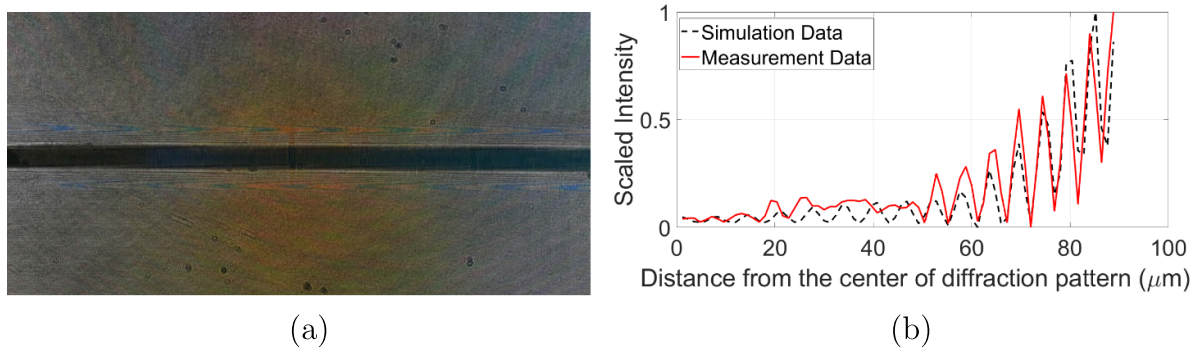


**Figure 5.** Non-coated optical fiber (a) experimental diffraction pattern (b) simulation and reconstruction of measurement data.

case, it penalizes large coefficients, dampening the model's flexibility.

After obtaining experimental data, we input the measurement data into the trained network. The columns of diffraction patterns were selected as the test data, and the rescaling process was performed without any filtering operation. Column selection was carried out by creating the columns with feature extraction, as visualized in figure 5(a). As a result, the 2D image file can be projected onto a 1D vector, and the computational load can be reduced. To further alleviate the computational burden of the algorithm, only half of the diffraction pattern is evaluated. Forty different vectors were utilized as the test data of the trained network to determine the coating thickness with an accuracy of 25 nm tolerance. The optical fibers have average thicknesses of non-coated, 140 nm, 235 nm, and 365 nm, all verified by SEM. The average coating thicknesses were determined by measuring various points on the samples. The SEM images of the four different optical fibers are given in figure 6.

In the final part, we classify and estimate the thickness of the transparent dielectric film using the network. Eighteen different classes with a sensitivity of 25 nm are created. The results obtained from the test data for the classification task are presented in figure 7. The actual curve is shown in red, while the output data is classified and assigned to one of the created classes. Generally, the output data is rounded, but in this case, we show unrounded results to facilitate the visualization.
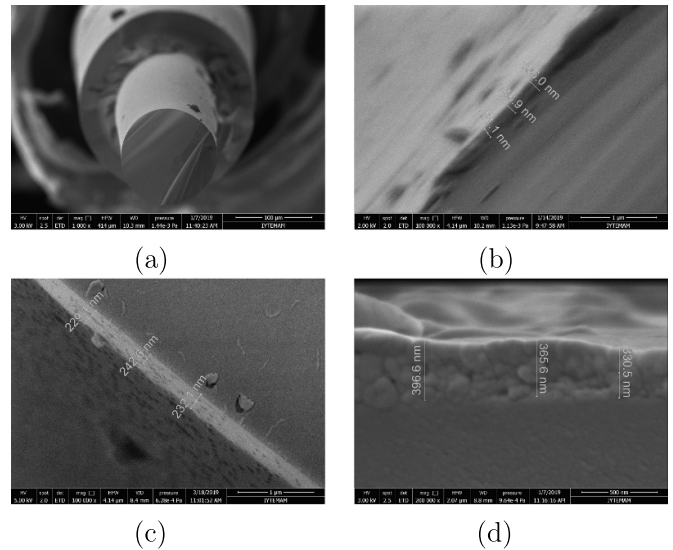


**Figure 6.** SEM images with average coating thickness: (a) non-coated (b) 140 nm (c) 235 nm (d) 365 nm.

Our analysis showed that 33 out of 40 data points belonged to the correct class, while only seven were assigned to an incorrect class, with a slight shift of only one unit. This demonstrates an 82.5% accuracy rate in the characterization of the coating thickness, which is a promising result for our network application.
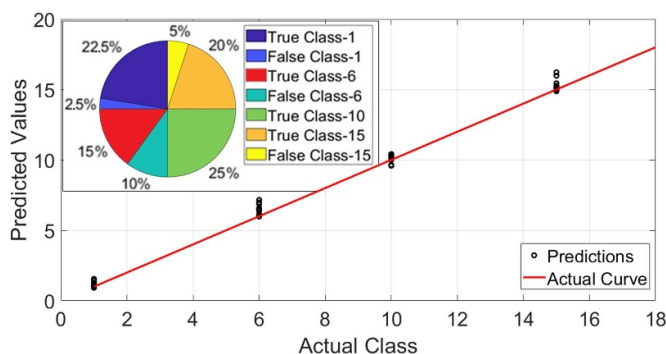
**Figure 7.** Results of experimental data.

## 5. Conclusion

This article presents an application of RBF neural network for the precise thickness identification of curved transparent dielectric films on the optical fiber. We have demonstrated that the conventional phase diffraction technique integrating with the RBF algorithm has huge potential to enhance thickness resolution significantly by reducing the radius of errors. Our experimental results show that the RBF network achieves an outstanding accuracy of 98% for 25 nm sensitivity, where half of the numerical simulation data is used for training and the other half for testing. Moreover, we examine noise effects in detail presenting parametric results. According to the observations, there is a particular threshold value for AWGN and a monotonic decrease curve for Poisson distribution noise. In the case of using experimental data for testing, the RBF network exhibits 82.5% accuracy for the same sensitivity value, primarily due to noise in the data. Our findings were also verified by destructive SEM measurements. As a result, the proposed approach is viable and efficient instead of traditional curve-matching methods for precisely estimating the thickness of transparent dielectric films in fiber optic sensor technologies.

## Data availability statement

The data cannot be made publicly available upon publication because no suitable repository exists for hosting data in this field of study. The data that support the findings of this study are available upon reasonable request from the authors.

## ORCID iDs

Enes Ataç ⬤ https://orcid.org/0000-0002-0694-610X
Anıl Karatay ⬤ https://orcid.org/0000-0002-4516-3028

## References

[1] Singh S and Gupta B D 2010 Simulation of a surface plasmon resonance-based fiber-optic sensor for gas sensing in visible range using films of nanocomposites *Meas. Sci. Technol.* **21** 115202

[2] Alwis L, Sun T and Grattan K T V 2013 Optical fibre-based sensor technology for humidity and moisture measurement: review of recent progress *Measurement* **46** 4052–74

[3] Wang B, Yuan Z, Lian C and Meng F 2023 A simultaneous distinguishing measurement method of carbon dioxide gas concentration and air humidity based on double fiber bragg gratings *IEEE Trans. Instrum. Meas.* **72** 7004310

[4] Wang Y, Li J, Guo L-N, Tian M and Meng F 2023 Development of fabrication technique and sensing performance of optical fiber humidity sensors in the most recent decade *Measurement* **215** 112888

[5] Mishra S K, Usha S P and Gupta B D 2016 A lossy mode resonance-based fiber optic hydrogen gas sensor for room temperature using coatings of ITO thin film and nanoparticles *Meas. Sci. Technol.* **27** 045103

[6] Mishra V, Lohar M and Amphawan A 2016 Improvement in temperature sensitivity of FBG by coating of different materials *Optik* **127** 825–8

[7] Gong P, Li X, Zhou X, Zhang Y, Chen N, Wang S, Zhang S and Zhao Y 2021 Optical fiber sensors for glucose concentration measurement: a review *Opt. Laser Technol.* **139** 106981

[8] Yang M and Dai J 2012 Review on optical fiber sensors with sensitive thin films *Photon. Sens.* **2** 14–28

[9] Liang H, Wang J, Zhang L, Liu J and Wang S 2022 Review of optical fiber sensors for temperature, salinity and pressure sensing and measurement in seawater *Sensors* **22** 5363

[10] Johnson Singh M, Choudhary S, Chen W-B, Wu P-C, Kumar Goyal M, Rajput A and Borana L 2023 Applications of fibre bragg grating sensors for monitoring geotechnical structures: a comprehensive review *Measurement* **218** 113171

[11] Swanson A J, Raymond S G, Janssens S, Breukers R D, Bhuiyan M D H, Lovell-Smith J W and Waterland M R 2015 Investigation of polyimide coated fibre bragg gratings for relative humidity sensing *Meas. Sci. Technol.* **26** 125101

[12] Li C, Yang W, Wang M, Yu X, Fan J, Xiong Y, Yang Y and Li L 2020 A review of coating materials used to improve the performance of optical fiber sensors *Sensors* **20** 4215

[13] Wang Y, Dong J, Luo Y, Tang J, Lu H, Yu J, Guan H, Zhang J and Chen Z 2017 Indium tin oxide coated two-mode fiber for enhanced SPR sensor in near-infrared region *IEEE Photon. J.* **9** 1–9

[14] Cheng H, Wang Li, Xiao R and Wang J 2022 Temperature sensing of π-PSFBG with ITO film coated by PLD method *Optik* **262** 169289

[15] Zhang X, Alemohammad H and Toyserkani E 2013 Sensitivity alteration of fiber Bragg grating sensors with additive micro-scale bi-material coatings *Meas. Sci. Technol.* **24** 025106

[16] Ghim Y-S, Rhee H-G, Yang H-S and Lee Y-W 2013 Thin-film thickness profile measurement using a Mirau-type low-coherence interferometer *Meas. Sci. Technol.* **24** 075002

[17] Kim M-G 2022 Spectroscopic imaging ellipsometry for two-dimensional thin film thickness measurement using a digital light processing projector *Meas. Sci. Technol.* **33** 095016

[18] Ohlídal M, Ohlídal I, Klapetek P, Nečas D and Majumdar A 2011 Measurement of the thickness distribution and optical constants of non-uniform thin films *Meas. Sci. Technol.* **22** 085104

[19] Kim M-G 2018 Improvement of spectral resolution in spectroscopic imaging reflectometer using rotating-type filter and tunable aperture *Meas. Sci. Technol.* **29** 105001

[20] Kumar Debnath S K, You J and Kim S-W 2009 Determination of film thickness and surface profile using reflectometry and spectrally resolved phase shifting interferometry *Int. J. Precis. Eng. Manuf.* **10** 5–10

[21] Yoshino H, Abbas A, Kaminski P M, Smith R, Walls J M and Mansfield D 2017 Measurement of thin film interfacial surface roughness by coherence scanning interferometry *J. Appl. Phys.* **121** 105303

[22] Zhu Y, Li Z, Lu X, Yuan Y and Yang J 2022 White light interferometry with spectral-temporal demodulation for large-range thickness measurement *Chin. Opt. Lett.* **20** 091201

[23] Ekici Çağın and Dinleyici M S 2017 A practical approach for optical characterization of a film coated on the optical fiber *Opt. Fiber Technol.* **36** 382–6

[24] Ataç E and Dinleyici M S 2020 Nanoscale curved dielectric film characterization beyond diffraction limits using spatially structured illumination *Opt. Fiber Technol.* **58** 102267

[25] Tavassoly M T, Darudi A, Reza Khalesifard H and Hosseini S M R S 2001 Applications of Fresnel diffraction from phase objects *Proc. SPIE* **4399** 98–106

[26] Tavassoly M T, Roohollah Hosseini S R, Motazedi Fard A M and Rezvani Naraghi R R 2012 Applications of Fresnel diffraction from the edge of a transparent plate in transmission *Appl. Opt.* **51** 7170–5

[27] Bui N-T *et al* 2022 Improved accuracy of optical distance sensor based on artificial neural network applied to real-time systems *Meas. Sci. Technol.* **33** 075001

[28] Choe J, Jon S, Ryang W, Yun Y and So J 2022 Research of laser ultrasonic defect statistics recognition technology based on radial basis function neural network *Opt. Laser Technol.* **150** 107857

[29] Du X, Jia M, Huang S, Sun Z, Tian Y, Chai Q, Li W and Zhang J 2023 Event identification based on sample feature correction algorithm for $\phi$-otdr *Meas. Sci. Technol.* **34** 085120

[30] Chiu P-H, Lin Y-S, Chanie Manie Y C, Li J-W, Lin J-H and Peng P-C 2021 Intensity and wavelength-division multiplexing fiber sensor interrogation using a combination of autoencoder pre-trained convolution neural network and differential evolution algorithm *IEEE Photon. J.* **13** 1–9

[31] Liehr S, Ann Jäger L, Karapanagiotis C, Münzenberger S and Kowarik S 2019 Real-time dynamic strain sensing in optical fibers using artificial neural networks *Opt. Express* **27** 7405–25

[32] Jia Z, Ren L, Li H and Sun W 2018 Pipeline leak localization based on FBG hoop strain sensors combined with BP neural network *Appl. Sci.* **8** 146

[33] Kowarik S, Hussels M-T, Chruscicki S, Münzenberger S, Lämmerhirt A, Pohl P and Schubert M 2020 Fiber optic train monitoring with distributed acoustic sensing: Conventional and neural network data analysis *Sensors* **20** 450

[34] Wang B, Mao Y, Ashry I, Al-Fehaid Y, Al-Shawaf A, Ng T K, Yu C and Ooi B S 2021 Towards detecting red palm weevil using machine learning and fiber optic distributed acoustic sensing *Sensors* **21** 1592

[35] Kalam Azad A, Wang L, Guo N, Tam H-Y and Lu C 2016 Signal processing using artificial neural network for BOTDA sensor system *Opt. Express* **24** 6769–82

[36] Lu S, Tan Z, Li G and Yang J 2021 A sensitized plastic fiber sensor for multi-point bending measurement based on deep learning *IEEE Photon. J.* **13** 1–7

[37] Eriksson T A, Bülow H and Leven A 2017 Applying neural networks in optical communication systems: possible pitfalls *IEEE Photonics Technol. Lett.* **29** 2091–4

[38] Lohani S, Knutson E M, O'Donnell M, Huver S D and Glasser R T 2018 On the use of deep neural networks in optical communications *Appl. Opt.* **57** 4180–90

[39] Chuang C-Y, Liu Li-C, Wei C-C, Liu J-J, Henrickson L, Wang C-L, Chen Y-K and Chen J 2018 Study of training patterns for employing deep neural networks in optical communication systems *2018 European Conf. on Optical Communication* (*ECOC*) (IEEE) pp 1–3

[40] Lee B, Yu K, Jeon J and Choi E J 2022 Machine learning analysis of broadband optical reflectivity of semiconductor thin film *J. Korean Phys. Soc.* **80** 347–51

[41] Tsui S-Y, Wang C-Y, Huang T-H and Sung K-B 2018 Modelling spatially-resolved diffuse reflectance spectra of a multi-layered skin model by artificial neural networks trained with Monte Carlo simulations *Biomed. Opt. Express* **9** 1531–44

[42] Cowie B M, Webb D J, Tam B, Slack P and Brett P N 2006 Fibre Bragg grating sensors for distributive tactile sensing *Meas. Sci. Technol.* **18** 138

[43] Shao Y, Chen C, Lu Z, Zheng Y and Zhang Y 2022 An intelligent leakage detection method for diaphragm wall joints based on fiber Bragg grating sensors and intelligent algorithms *Measurement* **197** 111339

[44] Kim M-G 2020 Improved measurement of thin film thickness in spectroscopic reflectometer using convolutional neural networks *Int. J. Precis. Eng. Manuf.* **21** 219–25

[45] Choi J E and Hong S J 2021 Machine learning-based virtual metrology on film thickness in amorphous carbon layer deposition process *Meas. Sens.* **16** 100046

[46] Makris K G and Psaltis D 2011 Huygens-Fresnel diffraction and evanescent waves *Opt. Commun.* **284** 1686–9

[47] Baughman D R and Liu Y A 1995 Classification: fault diagnosis and feature categorization *Neural Networks in Bioprocessing and Chemical Engineering* (Academic) pp 110–71

[48] Piscaer P J, Gupta A, Soloviev O and Verhaegen M 2018 Modal-based phase retrieval using Gaussian radial basis functions *J. Opt. Soc. Am.* A **35** 1233–42

[49] Martinez-Finkelshtein A, Ramos-Lopez D and Iskander D R 2017 Computation of 2d Fourier transforms and diffraction integrals using Gaussian radial basis functions *Appl. Comput. Harmon. Anal.* **43** 424–48

[50] Trahan R and Hyland D 2013 Phase retrieval of images using Gaussian radial bases *Appl. Opt.* **52** 8627–33

[51] Gurney K 2018 *An Introduction to Neural Networks* (CRC Press)

[52] Sammut C and Webb G I 2010 Mean squared error *Encyclopedia of Machine Learning* (Springer) p 653

[53] Richardson J J, Cui J, Bjornmalm M, Braunger J A, Ejima H and Caruso F 2016 Innovation in layer-by-layer assembly *Chem. Rev.* **116** 14828–67

[54] Zhang X, Xu Y, Zhang X, Wu H, Shen J, Chen R, Xiong Y, Li J and Guo S 2019 Progress on the layer-by-layer assembly of multilayered polymer composites: strategy, structural control and applications *Prog. Polym. Sci.* **89** 76–107

[55] Zhao S *et al* 2019 The future of layer-by-layer assembly: a tribute to acs nano associate editor Helmuth Mohwald *ACS Nano* **13** 6151–69